

Orientation Dynamics of Sedimenting Anisotropic Particles in Turbulence

Prateek Anand^{1,*}, Samriddhi Sankar Ray^{2,†}, and Ganesh Subramanian^{1,‡}

¹Jawaharlal Nehru Centre for Advanced Scientific Research, Bangalore 560064, India

²International Centre for Theoretical Sciences, Tata Institute of Fundamental Research, Bangalore 560089, India



(Received 23 August 2019; revised 12 May 2020; accepted 19 June 2020; published 13 July 2020)

We examine the dynamics of small anisotropic particles (spheroids) sedimenting through homogeneous isotropic turbulence using direct numerical simulations and theory. The gravity-induced inertial torque acting on sub-Kolmogorov spheroids leads to pronouncedly non-Gaussian orientation distributions localized about the broadside-on (to gravity) orientation. Orientation distributions and average settling velocities are obtained over a wide range of spheroid aspect ratios, Stokes, and Froude numbers. Orientational moments from the simulations compare well with analytical predictions in the inertialess rapid-settling limit, with both exhibiting a nonmonotonic dependence on spheroid aspect ratio. Deviations arise at Stokes numbers of order unity due to a spatially inhomogeneous particle concentration field resulting from a preferential sweeping effect; as a consequence, the time-averaged particle settling velocities exceed the orientationally averaged estimates.

DOI: 10.1103/PhysRevLett.125.034501

Suspended inertial anisotropic particles show up in a variety of scenarios ranging from pollen dispersion to soot emission. Prominent examples in nature include ice crystals suspended in high-altitude cirrus clouds which are a crucial element in the planetary greenhouse effect [1,2]. The radiative properties of such clouds depend sensitively on the orientation distribution of ice crystals [3]. The latter come in a variety of pristine shapes with sizes ranging from tens to thousands of microns [4], smaller than the typical Kolmogorov scales, about a millimeter, for atmospheric turbulence. Therefore, a first step towards understanding Cirrus cloud radiation is to examine how sub-Kolmogorov anisotropic particles orient themselves while sedimenting in a turbulent flow.

The critical role of turbulence in gravitational settling has been investigated in-depth only for inertial *spherical* particles [5–7]. In this simpler scenario, relevant to the dynamics of water droplets in warm clouds, for instance, we now have a detailed understanding of the role of turbulence in enhancing single-particle sedimentation [8–10] as well as collision [11–16] and coalescence [17] rates which control raindrop formation [18,19].

The effect of inertia for anisotropic particles is far more involved owing to additional rotational degrees of freedom [20]. Most earlier studies ignore either inertia [21,22] (the suspended particles acting as probes for the turbulent velocity-gradient tensor [20,23]) or gravity [24,25]. Experiments have also largely focussed on neutrally buoyant anisotropic tracers in turbulence [26–28]. Thus, gravitational settling of heavy anisotropic particles, beyond simple laminar flows under Stokesian conditions [29,30], remains largely unexplored [20]. Recent efforts address the issue of how such particles sediment in nontrivial flows [31–34], but the effect of gravity

on rotational dynamics is not accounted for, leading to orientation distributions that are far from being representative. There exist efforts analyzing the motion of anisotropic particles in turbulent channel flow, the object of interest often being the particle deposition rate onto walls [35–39]. Gravity is omitted in most of these efforts; those that do include gravity again neglect its role in the rotational dynamics [40]. In this work, using direct numerical simulations (DNSs) and theory, we characterize the distribution of particle orientations in suspensions of spheroids sedimenting in an ambient homogeneous isotropic turbulent field. Rigorously accounting for the effects of gravity on both the particle translational and rotational degrees of freedom, we find, in contrast to earlier efforts [31–34], that the orientation distributions always peak at the broadside-on (to gravity) orientation. Further, although the particle settling velocities equal the orientationally averaged estimates in the rapid-settling limit, they consistently exceed the latter when effects of particle inertia become significant.

We perform direct numerical simulations of noninteracting spheroids sedimenting through homogeneous isotropic turbulence with a mass loading assumed small enough for carrier-fluid turbulence to remain unaffected (a one-way coupled framework) [41]. The fluid velocity and pressure fields satisfy the incompressible Navier-Stokes equations for a fluid with density ρ_f and kinematic viscosity ν . Turbulence is maintained in a statistically stationary homogeneous isotropic state via injection of energy at the lowest wave numbers ($1 \leq k_f \leq 2$) [49]. The simulations are pseudospectral in space and involve a second-order Adams-Bashforth scheme for time marching. A spatial resolution of 512^3 collocation points is used, with the choice of four different kinematic viscosities corresponding to Taylor-scale

Reynolds numbers, $R_\lambda = u_{\text{rms}}^2 \sqrt{15/\epsilon\nu}$, of 47, 96, 150, and 200 (u_{rms} is the root-mean-square velocity and $\epsilon = 2\nu\langle\mathbf{E}:\mathbf{E}\rangle$ is the averaged dissipation rate). For each R_λ , we follow the motion of 100000 oblate (prolate) spheroids, with aspect ratios (κ) ranging from 0.1 to 0.01 (10 to 100); here, $\kappa = a/b$, a and b being the semiaxis lengths along and orthogonal to the spheroid symmetry axis \mathbf{p} . The particles are initialized at random positions with their translational velocities set equal to fluid values and angular velocities set equal to those of anisotropic tracers [50] at their locations. The initial orientations, as characterized by normalized quaternions [51], are uniformly distributed over the unit sphere. The simulations are run for 5–6 integral-scale eddy turnover times, sufficient to attain a statistical steady state.

The equations governing the particle dynamics are

$$\begin{aligned} \frac{d\mathbf{U}_p}{dt} &= \mathbf{g} + \frac{1}{\tau_p X_A} \mathbf{M}_t^{-1} \cdot (\mathbf{u} - \mathbf{U}_p), \quad (1) \\ \frac{d\boldsymbol{\omega}_p}{dt} &+ \mathbf{I}_p^{-1} \cdot [\boldsymbol{\omega}_p \wedge (\mathbf{I}_p \cdot \boldsymbol{\omega}_p)] \\ &= K_{\text{sed}} \mathbf{I}_p^{-1} \cdot [(\mathbf{M}_t \cdot \hat{\mathbf{g}}) \cdot \mathbf{p} (\mathbf{M}_t \cdot \hat{\mathbf{g}}) \wedge \mathbf{p}] \\ &+ 8\pi\mu L^3 \mathbf{I}_p^{-1} \cdot [\mathbf{M}_r^{-1} \cdot \left(\frac{1}{2}\boldsymbol{\Omega} - \boldsymbol{\omega}_p\right) - Y_H(\mathbf{E} \cdot \mathbf{p}) \wedge \mathbf{p}], \quad (2) \end{aligned}$$

where \mathbf{U}_p and $\boldsymbol{\omega}_p$ are the translational and angular velocities of the particles, \mathbf{g} is the gravitational acceleration ($\hat{\mathbf{g}}$ being the corresponding unit vector), L is the largest particle dimension, and τ_p is the particle relaxation time (see Ref. [41]). \mathbf{I}_p in Eq. (2) is the moment of inertia tensor, while \mathbf{M}_t and \mathbf{M}_r denote the Stokesian translational and rotational mobility tensors for the spheroid, with $\mathbf{M}_{t(r)} = X_{A(C)}^{-1}(\kappa)\mathbf{pp} + Y_{A(C)}^{-1}(\kappa)(\mathbf{I} - \mathbf{pp})$, the principal resistance coefficients ($X_A - Y_C$) being well-known functions of κ [52]. The large particle-to-fluid density ratio (ρ_p/ρ_f), relevant to the atmospheric scenario, implies the neglect of Basset and added mass forces in Eq. (1). The particle Reynolds numbers based on both the Kolmogorov shear rate [$\dot{\gamma}_\eta = (\epsilon/\nu)^{1/2}$] and the nominal slip velocity ($U_s = \tau_p g$) are assumed small ($\text{Re}_{\dot{\gamma}_\eta} = \dot{\gamma}_\eta L^2/\nu$, $\text{Re}_s = U_s L/\nu < 1$), so particles are acted on, at leading order, by the sum of the gravitational force and quasisteady Stokes drag proportional to the slip velocity [53]; see Ref. [41]. Since sub-Kolmogorov spheroids experience turbulence as a fluctuating linear flow, the Jeffery relation [50,52] is used for the turbulent torque in Eq. (2) with the ratio $Y_H/Y_C = (\kappa^2 - 1)/(\kappa^2 + 1)$ being the Bretherton constant B [54]. Equation (2) includes, in addition, the gravity-induced torque acting to orient an anisotropic particle, sedimenting in a quiescent fluid at small but finite Re_s , broadside-on to gravity [55–57]; an expression for this torque was obtained in Ref. [55]. The superposition of the gravity and shear-induced torques in Eq. (2) has been used [58]

earlier to determine the orientation dynamics of particles sedimenting through simple shear flow [59,60]. The quantity $\text{TR} = (K_{\text{sed}}/\mu L^3 \dot{\gamma}_\eta) \sim \text{Fr}_\eta^2 f_I(\kappa)$ characterizes the relative magnitudes of these torques in Eq. (2), where $K_{\text{sed}} = \text{Re}_s \mu U_s L^2 f_I(\kappa) X_A^2$, with the aspect-ratio dependent function, $f_I(\kappa)$, having been obtained in Ref. [55], and $\text{Fr}_\eta = \tau_p g/u_\eta$ being the Froude number based on the Kolmogorov velocity scale ($u_\eta = (\nu\epsilon)^{1/3}$). In Eq. (1) and Eq. (2), \mathbf{u} , $\boldsymbol{\Omega}$, and \mathbf{E} denote the undisturbed turbulent velocity, vorticity, and rate-of-strain fields interpolated at the particle positions [41].

Apart from R_λ , κ , and Fr_η , the dynamics as governed by Eq. (1) and Eq. (2), on length scales of the order of the Kolmogorov scale [$l_\eta = (\nu^3/\epsilon)^{1/4}$] or smaller, is a function of the Kolmogorov Stokes number ($\text{St}_\eta = \tau_p/\tau_\eta$ with $\tau_\eta = \dot{\gamma}_\eta^{-1}$ the Kolmogorov time scale). Using parameters characteristic of the atmospheric scenario, including ice crystal sizes and turbulence dissipation rates from Ref. [34], the simulations reported here correspond to $\text{St}_\eta \in (0.0037, 0.4)$ and $\text{Fr}_\eta \in (0.5, 17)$. For a given R_λ , the dynamics of the thinnest (disklike) spheroids corresponds to the smallest Stokes and Froude numbers. The torque ratio, TR ranges from 1–800 for all ice crystal sizes and turbulence intensities considered here. Thus, the gravity-induced torque is expected to be dominant for typical ice clouds. This is borne out in Fig. 1 which shows the distribution of orientations $\cos\theta_0 = |\hat{\mathbf{g}} \cdot \mathbf{p}|$ (since \mathbf{p} and $-\mathbf{p}$ correspond to the same spheroid orientation, we take the modulus), obtained from our DNSs for (a) $R_\lambda = 150$ and (b) $R_\lambda = 47$. For each R_λ , we show results for oblate spheroids of different aspect ratios (see legend), both with ($\text{Re}_s = 0.8$) and without ($\text{Re}_s = 0$) the gravity-induced torque. The gravity-induced torque causes the distributions to be sharply localized about the broadside-on orientation ($\cos\theta_0 = 1$), especially for the smaller R_λ . In contrast, as emphasized in the insets of Fig. 1, neglect of this torque leads to distributions peaked at the longside-on orientation ($\cos\theta_0 = 0$ for oblate spheroids), although this maximum is quite shallow, consistent with earlier studies [32–34]. The continuous curves in Fig. 1 are a guide to the eye; the comparison with a Gaussian in Fig. 1(a) nevertheless conveys the pronouncedly non-Gaussian character of the distributions for $\text{Re}_s = 0.8$.

Analytical progress is possible in the rapid-settling limit (henceforth, RST or “rapid-settling theory”), $l_\eta/U_s \ll \tau_\eta$ or $\text{Fr}_\eta \gg 1$, when a particle settles through a Kolmogorov eddy much faster than the eddy decorrelates [61] (see Ref. [41]). Further, assuming $\text{St}_\eta \ll 1$, and neglecting the angular acceleration in Eq. (2), the rate of change of spheroid orientation, $\dot{\mathbf{p}} = \boldsymbol{\omega}_p \wedge \mathbf{p}$, is given by

$$\begin{aligned} \dot{\mathbf{p}} &= -\mathbf{M}_r \cdot [K_{\text{sed}}[(\mathbf{M}_t \cdot \hat{\mathbf{g}}) \cdot \mathbf{p} (\mathbf{M}_t \cdot \hat{\mathbf{g}})] \wedge \mathbf{p}] \wedge \mathbf{p} \\ &+ \frac{1}{2}\boldsymbol{\Omega} \wedge \mathbf{p} + \frac{Y_H}{Y_C} [\mathbf{E} \cdot \mathbf{p} - \mathbf{E} : \mathbf{ppp}]. \quad (3) \end{aligned}$$

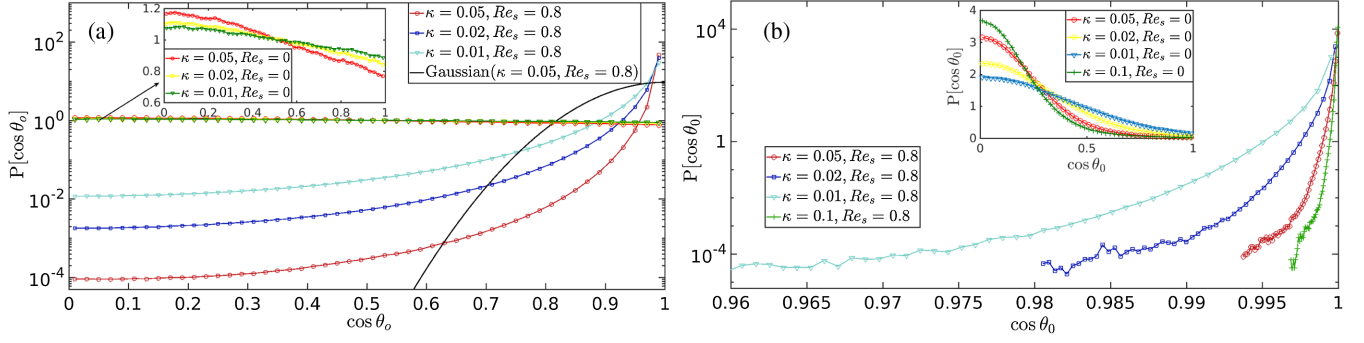


FIG. 1. Probability distributions of $|\mathbf{p} \cdot \hat{\mathbf{g}}|$ for (a) $R_\lambda = 150$ and (b) $R_\lambda = 47$ in the presence ($Re_s = 0.8$) and (inset) absence ($Re_s = 0$) of a gravity-induced torque; different curves correspond to different κ (see legend). The solid black line in (a) denotes a Gaussian with the same second moment as the distribution for $\kappa = 0.05$, $Re_s = 0.8$.

As already seen, the torque ratio $TR \sim f_I(\kappa)Fr_\eta^2$ with $f_I(\kappa) \sim \mathcal{O}(1)$ for oblate spheroids. For large Fr_η , the weak turbulent shear only leads to small fluctuations about the broadside-on orientation. For such orientations, with $\hat{\mathbf{g}} = \mathbf{I}_3$, one has $\mathbf{p} \cdot \hat{\mathbf{g}} = p_3 \approx 1$ and $p_{1,2} \ll 1$. Furthermore, the rotation rate of the nearly broadside-on spheroid, in any plane containing $\hat{\mathbf{g}}$, is asymptotically small since the gravity-induced torque vanishes for the broadside-on orientation. Thus, there is a near-balance between the 1 and 2 components of the turbulent and gravity-induced torques at leading order, the terms proportional to $\dot{p}_{1,2}$ in Eq. (3) being $\mathcal{O}(Fr_\eta^{-2})$ smaller. This gives

$$\mathbf{p} \cdot (\mathbf{I} - \hat{\mathbf{g}}\hat{\mathbf{g}}) \approx \frac{1}{Fr_\eta^2} \frac{8\pi Y_A Y_c \tau_\eta}{f_I(\kappa) X_A} \left(\mathbf{S} + \frac{Y_H}{Y_c} \mathbf{E} \right) \cdot \mathbf{p} \quad (4)$$

for the projection of the spheroid axis in the plane transverse to gravity; here $\mathbf{S} = \frac{1}{2}\boldsymbol{\epsilon} \cdot \boldsymbol{\Omega}$ is the vorticity tensor and $\boldsymbol{\epsilon}$ being the Levi-Civita symbol. The components $p_{1,2}$ transverse to gravity are linear functionals of the turbulent velocity gradient tensor. Turbulent velocity gradients are dominated by the smallest (Kolmogorov) scales, and are pronouncedly non-Gaussian [62]; hence the orientation distributions, in the rapid-settling limit, are non-Gaussian

(characterized below via the second and fourth moments) despite the localization about the broadside-on orientation.

Since $p_3 = \cos \theta_0 \approx 1 - (\theta_0^2/2)$ for $\theta_0 \ll 1$, $\langle 1 - p_3^2 \rangle = \langle p_1^2 + p_2^2 \rangle \approx \langle \theta_0^2 \rangle$ corresponds to the variance of the orientation distribution about the broadside-on orientation. With $p_{1,2}$ linear in \mathbf{E} and \mathbf{S} , calculating $\langle 1 - p_3^2 \rangle$ requires the variance of the turbulent rate of strain and vorticity tensors over a particle settling trajectory. For $St_\eta \ll 1$, $Fr_\eta \gg 1$, one expects no preferential sampling and the average along a settling trajectory, $\langle \dots \rangle$, above may be replaced by the usual fluid ensemble average [63]. For homogeneous isotropic turbulence, the ensemble averages are $\langle E_{ij}E_{kl} \rangle = (\dot{\gamma}_\eta^2/20)(\delta_{ik}\delta_{jl} + \delta_{il}\delta_{jk} - \frac{2}{3}\delta_{ij}\delta_{kl})$, $\langle S_{ij}S_{kl} \rangle = (\dot{\gamma}_\eta^2/12)(\delta_{ik}\delta_{jl} - \delta_{il}\delta_{jk})$, and $\langle S_{ij}E_{kl} \rangle = 0$ [64,65]. Using these [41], one finds

$$\langle 1 - p_3^2 \rangle \approx \frac{32\pi^2 Y_A^2 Y_c^2}{f_I^2(\kappa) X_A^2} \left(\frac{1}{3} + \frac{Y_H^2}{5Y_c^2} \right) \frac{1}{Fr_\eta^4}. \quad (5)$$

Figure 2(a) compares the DNS results for $\langle 1 - p_3^2 \rangle$ to Eq. (5) and demonstrates the good agreement for large Fr_η , with deviations arising for Fr_η of order unity and smaller, in which case $\langle 1 - p_3^2 \rangle$ approaches a plateau.

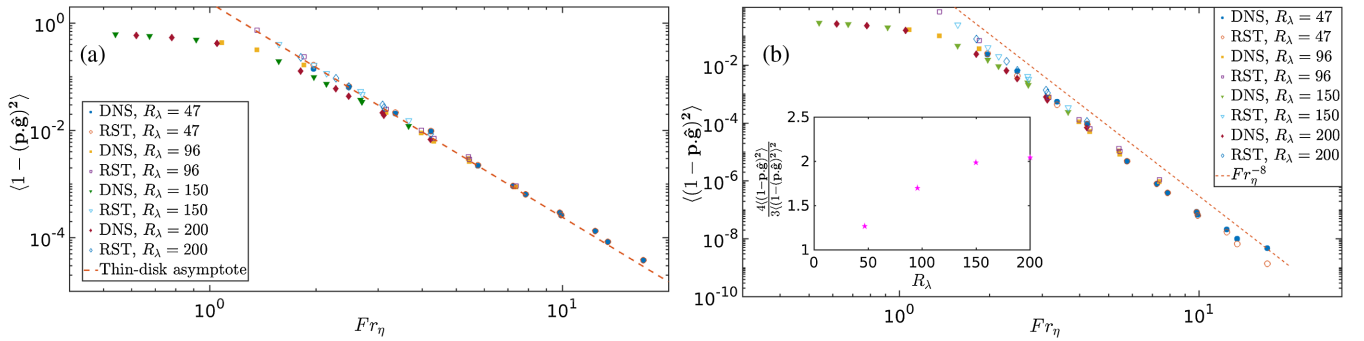


FIG. 2. Comparison of the orientation moments (a) $\langle 1 - (\mathbf{p} \cdot \hat{\mathbf{g}})^2 \rangle$ and (b) $\langle (1 - \mathbf{p} \cdot \hat{\mathbf{g}})^2 \rangle$ obtained from DNSs with RST predictions [Eqs. (5) and (6)] in the rapid-settling limit ($Fr_\eta \gg 1$). The inset in panel (b) is a measure (see text) of the departure from Gaussianity of the orientation distributions.

A more sensitive measure of the orientation distributions is $\langle(1 - p_3)^2\rangle$. For a distribution localized about the broadside-on orientation, $\langle(1 - p_3)^2\rangle \propto \langle\theta_0^4\rangle$, and is therefore a measure of the fourth moment. Proceeding along lines sketched above, $\langle(1 - p_3)^2\rangle \approx \frac{1}{4}\langle(p_1^2 + p_2^2)^2\rangle$ with $p_{1,2}$ as given above, and the calculation involves the fourth moment of the turbulent velocity gradient tensor [41]. One obtains

$$\langle(1 - p_3)^2\rangle \approx \frac{1}{4} \left(\frac{8\pi Y_A Y_c}{f_I(\kappa) X_A} \right)^4 [M_1 + B^2 M_2 + B^4 M_3] \frac{1}{Fr_\eta^8}, \quad (6)$$

where $M_1 = (3G_1/2) + (32G_2/15) - (162G_3/15)$, $M_2 = -3G_1 + (8G_2/15) + (54G_3/5)$ and $M_3 = (3G_1/2)$, with $G_1 = \langle(\tau_\eta \partial u_1 / \partial x_1)^4\rangle$, $G_2 = \langle(\tau_\eta \partial u_1 / \partial x_2)^4\rangle$ and $G_3 = \langle\tau_\eta^4 (\partial u_1 / \partial x_1)^2 (\partial u_1 / \partial x_2)^2\rangle$ being the independent (non-dimensional) scalar components involving the fourth moment of the velocity gradient. Unlike the second moment, the prefactor multiplying Fr_η^{-8} is both a function of κ and R_λ , the latter dependence arising from dissipation-range intermittency referred to above. Figure 2(b) compares Eq. (6) with DNS results, the pattern of agreement being similar to that of the second moment above [66]. Since $\langle 1 - p_3^2 \rangle = \langle \theta_0^2 \rangle$ and $\langle (1 - p_3)^2 \rangle = \frac{1}{4} \langle \theta_0^4 \rangle$ for large Fr_η , the ratio $\{[4\langle(1 - p_3)^2\rangle]/[3\langle 1 - p_3^2 \rangle]\}$, which is independent of Fr_η , characterizes the departure from Gaussianity. This ratio, which is unity for a Gaussian, is plotted as an inset in Fig. 2(b) for $\kappa \rightarrow 0$ (a flat disk); it is well above unity and increases with increasing R_λ . One therefore expects orientation distributions in the atmospheric case, with R_λ 's 1 to 2 orders of magnitude higher than those in our simulations [19], to have similar variances but be significantly more intermittent.

In the inset of Fig. 3, we plot orientation distributions as a function of the spheroid aspect ratio, other physical

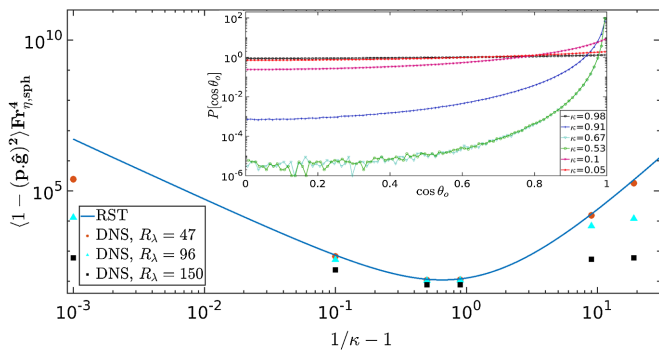


FIG. 3. Orientation distributions for $R_\lambda = 96$ for various aspect ratios, all other parameters staying fixed (see Ref. [41]). The inset highlights the nonmonotonic behavior of the second moment, $\langle(1 - (\mathbf{p} \cdot \hat{\mathbf{g}})^2)\rangle$, scaled with $Fr_{\eta, \text{sph}}^4$, when plotted as a function of κ for $R_\lambda = 47, 96$, and 150.

parameters being fixed [41]. Interestingly, the localization about the broadside-on orientation first increases as κ increases from zero (a flat disk), attains a maximum, before decreasing again as κ approaches unity. The non-monotonicity arises because the gravity-induced torque is small for both flat disks (due to the vanishingly small mass of such shapes) and near-spheres (since the torque scales with the square of the small eccentricity). The second moment from the RST framework, Eq. (5), can be rewritten to isolate the κ dependence through a change of variable $Fr_\eta = Fr_{\eta, \text{sph}} * (\kappa/X_A)$, where $Fr_{\eta, \text{sph}} = (2\rho_p L^2 g / 9\mu u_\eta)$. The resulting κ dependence is consistent with the above non-monotonicity; although, within the RST framework, $\langle 1 - p_3^2 \rangle \sim \mathcal{O}(\kappa^{-4})$ for $\kappa \rightarrow 0$ and $\langle 1 - p_3^2 \rangle \sim \mathcal{O}(\kappa - 1)^{-2}$ for $\kappa \rightarrow 1$. Since $\langle 1 - p_3^2 \rangle \leq 1$, the divergences above betray a breakdown of the assumption of a localized distribution in the analysis. As shown in Fig. 3, the second moments from our DNS agree with Eq. (5) for intermediate values of κ (maximum localization of $\cos \theta_0$), but plateau in the aforementioned asymptotic limits (corresponding to a uniform distribution of $\cos \theta_0$). Overall, the disagreement with theory, expectedly, grows with increasing R_λ .

With increase in the turbulence intensity, Fr_η decreases while St_η increases to values of order unity. As already seen in Fig. 2, DNS results depart from RST predictions in this limit. A suspension of spherical particles in a turbulent flow is no longer spatially homogeneous when $Fr_\eta, St_\eta \sim \mathcal{O}(1)$ [10–12,67]. Preferential sampling of regions of low vorticity by inertial particles, together with a sweeping effect in presence of gravity, leads to enhanced settling velocities [8,9,68]. Figure 4 shows this to be true for the suspensions of spheroids considered here. For large Fr_η , the time-averaged settling speeds (which scale linearly with Fr_η on account of being proportional to the acceleration due to gravity) from the DNS agree with the orientational averages for $R_\lambda = 47$ and 96 (the Fr_η required for this agreement increases with increasing St_η). For finite Fr_η and St_η , the time averages consistently exceed the orientation averaged estimates due to the preferential sweeping effect [41].

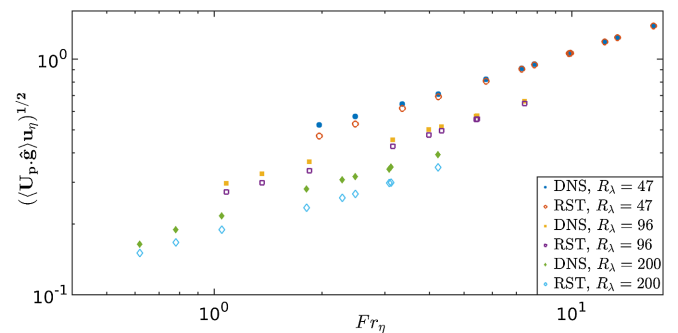


FIG. 4. Comparison between time-averaged and orientation-averaged settling speeds for $R_\lambda = 47, 96$, and 200.

In this Letter, we have characterized the orientation distributions and settling speeds of spheroids in homogeneous isotropic turbulence. Orientation distributions are localized about the broadside-on (to gravity) orientation, but are pronouncedly non-Gaussian for parameters typical of the atmospheric scenario. This is in contrast to recent studies which neglect the gravity-induced torque, and predict distributions peaked at the longside-on orientation [31–34]. The non-Gaussian distributions found here are also in contrast to earlier analyses reliant on a Gaussian ansatz [69,70]. While the broadside-on peak has been captured in Ref. [70], the simplistic Gaussian ansatz used for the velocity field, and the resulting Gaussian nature of the orientation fluctuations, is incorrect. Furthermore, Ref. [70] lacks any discussion on the spatial organization of the particles, and its effect on particle settling speeds. In contrast, we show that the particle concentration field remains homogeneous for $St_\eta \ll 1$; for $St_\eta \sim \mathcal{O}(1)$, preferential sweeping effects lead to a spatially inhomogeneous concentration and enhanced settling speeds (Fig. 4, [41]). Results for prolate spheroids (not shown) are similar to those discussed above. It would be of interest, in the future, to characterize pair-level statistics for anisotropic particles in position-orientation space, as a step towards analyzing ice-water and ice-ice collision efficiencies; the latter thought of as crucial to explaining observed ice-crystal concentrations in mixed-phase clouds and relatively rapid snowflake formation in ice clouds [71–73].

S. S. R. acknowledges the financial support of the DAE, Government of India, under Project No. 12-R&D-TFR-5.10-1100 and DST (India) Project ECR/2015/000361. The simulations were performed on the ICTS clusters *Mowgli* and *Mario*, as well as the work stations from the project ECR/2015/000361: *Goopy* and *Bagha*. We would also like to thank JNCASR for financial support in providing the workstations that ran the simulations.

*prateek@jncasr.ac.in

†samriddhisankarray@gmail.com

*sganesh@jncasr.ac.in

- [1] K. N. Liou, *Cirrus clouds and climate*, in *McGraw-Hill Yearbook of Science and Technology* (McGraw-Hill, Columbus, OH, 2005), p. 432.
- [2] A. K. Pandit, H. S. Gadhavi, M. V. Ratnam, K. Raghunath, S. V. B. Rao, and A. Jayaraman, *Atmos. Chem. Phys.* **15**, 13833 (2015).
- [3] A. J. Baran and P. N. Francis, *Q. J. R. Meteorol. Soc.* **130**, 763 (2004).
- [4] M. W. Gallagher, P. J. Connolly, J. Whiteway, D. Figueras-Nieto, M. Flynn, T. W. Choullarton, K. N. Bower, C. Cook, R. Busen, and J. Hacker, *Q. J. R. Meteorol. Soc.* **131**, 1143 (2005).
- [5] P. A. Vaillancourt and M. K. Yau, *Bull. Am. Meteorol. Soc.* **81**, 285 (2000).
- [6] R. Monchaux, M. Bourgoïn, and A. Cartellier, *Int. J. Multiphase Flow* **40**, 1 (2012).
- [7] K. Gustavsson and B. Mehlig, *Adv. Phys.* **65**, 1 (2016).
- [8] M. R. Maxey, *J. Fluid Mech.* **174**, 441 (1987).
- [9] L. P. Wang and M. R. Maxey, *J. Fluid Mech.* **256**, 27 (1993).
- [10] J. Bec, H. Homann, and S. S. Ray, *Phys. Rev. Lett.* **112**, 184501 (2014).
- [11] P. J. Ireland, A. D. Bragg, and L. R. Collins, *J. Fluid Mech.* **796**, 617 (2016).
- [12] P. J. Ireland, A. D. Bragg, and L. R. Collins, *J. Fluid Mech.* **796**, 659 (2016).
- [13] L. P. Wang, O. Ayala, B. Rosa, and W. W. Grabowski, *New J. Phys.* **10**, 075013 (2008).
- [14] O. Ayala, B. Rosa, and L. P. Wang, *New J. Phys.* **10**, 075016 (2008).
- [15] E.-W. Saw, G. P. Bewley, E. Bodenschatz, S. S. Ray, and J. Bec, *Phys. Fluids* **26**, 111702 (2014).
- [16] M. James and S. S. Ray, *Sci. Rep.* **7**, 12231 (2017).
- [17] J. Bec, S. S. Ray, E.-W. Saw, and H. Homann, *Phys. Rev. E* **93**, 031102(R) (2016).
- [18] G. Falkovich, A. Fouxon, and M. G. Stepanov, *Nature (London)* **419**, 151 (2002).
- [19] R. A. Shaw, *Annu. Rev. Fluid Mech.* **35**, 183 (2003).
- [20] G. A. Voth and A. Soldati, *Annu. Rev. Fluid Mech.* **49**, 249 (2017).
- [21] A. Pumir and M. Wilkinson, *New J. Phys.* **13**, 093030 (2011).
- [22] A. Gupta, D. Vincenzi, and R. Pandit, *Phys. Rev. E* **89**, 021001(R) (2014).
- [23] C. Meneveau, *Annu. Rev. Fluid Mech.* **43**, 219 (2011).
- [24] A. Roy, A. Gupta, and S. S. Ray, *Phys. Rev. E* **98**, 021101(R) (2018).
- [25] A. Gupta, A. Roy, A. Saha, and S. S. Ray, *Phys. Rev. Fluids* **5**, 052601 (2020).
- [26] S. Parsa, E. Calzavarini, F. Toschi, and G. A. Voth, *Phys. Rev. Lett.* **109**, 134501 (2012).
- [27] S. Parsa and G. A. Voth, *Phys. Rev. Lett.* **112**, 024501 (2014).
- [28] S. Kramel, G. A. Voth, S. Tympel, and F. Toschi, *Phys. Rev. Lett.* **117**, 154501 (2016).
- [29] R. Mallier and M. R. Maxey, *Phys. Fluids A* **3**, 1481 (2002).
- [30] H. Shin and M. R. Maxey, *Phys. Rev. E* **56**, 5431 (1997).
- [31] K. Gustavsson, J. Jucha, A. Naso, E. L  v  que, A. Pumir, and B. Mehlig, *Phys. Rev. Lett.* **119**, 254501 (2017).
- [32] C. Siewert, R. P. J. Kunnen, M. Meinke, and W. Schroder, *Atmos. Res.* **142**, 45 (2014).
- [33] C. Siewert, R. P. J. Kunnen, and W. Schroder, *J. Fluid Mech.* **758**, 686 (2014).
- [34] J. Jucha, A. Naso, E. L  v  que, and A. Pumir, *Phys. Rev. Fluids* **3**, 014604 (2018).
- [35] F. Zhao and B. G. M. van Wachem, *Acta Mech.* **224**, 2331 (2013).
- [36] L. Zhao, C. Marchioli, and H. I. Andersson, *Phys. Fluids* **26**, 063302 (2014).
- [37] F.-G. Fan and G. Ahmadi, *J. Aerosol Sci.* **26**, 813 (1995).
- [38] P. H. Mortensen, H. I. Andersson, J. J. J. Gillissen, and B. J. Boersma, *Phys. Fluids* **20**, 093302 (2008).
- [39] K. O. Fong, O. Amili, and F. Coletti, *J. Fluid Mech.* **872**, 367 (2019).

- [40] H. Zhang, G. Ahmadi, F.-G. Fan, and J. B. McLaughlin, *Int. J. Multiphase Flow* **27**, 971 (2001).
- [41] See Supplemental Material at <http://link.aps.org/supplemental/10.1103/PhysRevLett.125.034501> for details, which includes Refs. [42–48].
- [42] G. Akiki, W. C. Moore, and S. Balachandar, *J. Comput. Phys.* **351**, 329 (2017).
- [43] A. H. Auer, Jr. and D. L. Veal, *J. Atmos. Sci.* **27**, 919 (1970).
- [44] J. A. K. Horwitz and A. Mani, *J. Comput. Phys.* **318**, 85 (2016).
- [45] N. Marath and G. Subramanian, *J. Fluid Mech.* **830**, 165 (2017).
- [46] H. R. Pruppacher and J. D. Klett, *Nature (London)* **284**, 88 (1980).
- [47] L. Schneiders, K. Fröhlich, M. Meinke, and W. Schröder, *J. Fluid Mech.* **875**, 520 (2019).
- [48] G. Subramanian and D. L. Koch, *Phys. Fluids* **18**, 073302 (2006).
- [49] M. Buzdicotti, A. Bhatnagar, L. Biferale, A. S. Lanotte, and S. S. Ray, *New J. Phys.* **18**, 113047 (2016).
- [50] G. B. Jeffery, *Proc. R. Soc. A* **102**, 161 (1922).
- [51] D. J. Evans and S. Murad, *Mol. Phys.* **34**, 327 (1977).
- [52] S. J. Kim and S. P. Karrila, *Microhydrodynamics: Principles and Selected Applications* (Butterworth-Heinemann, Boston, 1991).
- [53] The inertial correction to the Stokes drag is neglected here, being asymptotically small for the sub-Kolmogorov spheroids examined here. The correction is singular in nature, arising from length scales much larger than the particle size [55]. The scale is $\mathcal{O}(\nu/U_s)$ for the particle slip velocity being dominant ($\text{Re}_s \gg \text{Re}_{\dot{\gamma}_\eta}$), and $\mathcal{O}((\nu/\dot{\gamma}_\eta)^{1/2})$ for dominant shear ($\text{Re}_{\dot{\gamma}_\eta} \gg \text{Re}_s$), and the correction sensitively depends on the ratio $\text{Re}_s/\text{Re}_{\dot{\gamma}_\eta}^{1/2}$, even when both Reynolds numbers are asymptotically small [74,75].
- [54] F. P. Bretherton, *J. Fluid Mech.* **14**, 284 (1962).
- [55] V. Dabade, N. K. Marath, and G. Subramanian, *J. Fluid Mech.* **778**, 133 (2015).
- [56] R. G. Cox, *J. Fluid Mech.* **23**, 625 (1965).
- [57] R. E. Khayat and R. G. Cox, *J. Fluid Mech.* **209**, 435 (1989).
- [58] Unlike the drag [74,75], the gravity-induced torque arises as a regular inertial correction. For small Re_s and $\text{Re}_{\dot{\gamma}_\eta}$, the inertial torque that adds to the Jeffery torque in Eq. (2) is thus a linear superposition of the shear and gravity-induced contributions [59,60] (the shear-induced inertial contribution induces a drift across Stokesian Jeffery trajectories in a steady laminar setting [76–78]). The ratio of the shear to the gravitational torque is $\mathcal{O}(\text{Fr}_\eta^{-2})(L/l_\eta)^2$, and the former may be neglected for sub-Kolmogorov particles.
- [59] G. Subramanian and D. L. Koch, *J. Fluid Mech.* **535**, 383 (2005).
- [60] G. Subramanian and D. L. Koch, *J. Fluid Mech.* **557**, 257 (2006).
- [61] A. Roy, R. Hamati, L. Tierney, D. Koch, and G. Voth, *J. Fluid Mech.* **875**, 576 (2019).
- [62] This departure from Gaussianity is termed dissipation range intermittency [79–84].
- [63] G. K. Batchelor, *Theory of Homogeneous Isotropic Turbulence* (Cambridge University Press, Cambridge, England, 1953).
- [64] B. K. Brunk, D. L. Koch, and L. W. Lion, *Phys. Fluids* **9**, 2670 (1997).
- [65] S. B. Pope, *Turbulent Flows* (Cambridge University Press, Cambridge, England, 2000).
- [66] The two points in Fig. 2(b) which, despite having the two highest Fr_η , have poor agreement between the analytical and DNS values, correspond to the two shortest tails in Fig. 1(b). The simulation needs to run for longer times to capture these tails.
- [67] J. K. Eaton and J. R. Fessler, *Int. J. Multiphase Flow* **20**, 169 (1994).
- [68] G. H. Good, P. J. Ireland, G. P. Bewley, E. Bodenschatz, L. R. Collins, and Z. Warhaft, *J. Fluid Mech.* **759**, R3 (2014).
- [69] J. D. Klett, *J. Atmos. Sci.* **52**, 2276 (1995).
- [70] K. Gustavsson, M. Z. Sheikh, D. Lopez, A. Naso, A. Pumir, and B. Mehlig, *New J. Phys.* **21**, 083008 (2019).
- [71] A. P. Khain and I. K. Sednev, *Atmos. Res.* **36**, 107 (1995).
- [72] M. B. Pinsky and A. P. Khain, *Atmos. Res.* **47–48**, 69 (1998).
- [73] M. B. Pinsky and A. P. Khain, *J. Aerosol Sci.* **28**, 1177 (1997).
- [74] P. G. Saffman, *J. Fluid Mech.* **22**, 385 (1965).
- [75] J. B. McLaughlin, *J. Fluid Mech.* **224**, 261 (1991).
- [76] V. Dabade, N. K. Marath, and G. Subramanian, *J. Fluid Mech.* **791**, 631 (2016).
- [77] N. K. Marath, R. Dwivedi, and G. Subramanian, *J. Fluid Mech.* **811**, R3 (2017).
- [78] N. K. Marath and G. Subramanian, *J. Fluid Mech.* **844**, 357 (2018).
- [79] S. S. Ray, *Phys. Rev. Fluids* **3**, 072601(R) (2018).
- [80] Z.-S. She, *Fluid Dyn. Res.* **8**, 143 (1991).
- [81] J. Schumacher, J. D. Scheel, D. Krasnov, D. A. Donzis, V. Yakhot, and K. R. Sreenivasan, *Proc. Natl. Acad. Sci. U.S.A.* **111**, 10961 (2014).
- [82] U. Frisch, *Turbulence: The Legacy of A. N. Kolmogorov* (Cambridge University Press, Cambridge, England, 1995).
- [83] J. Schumacher, K. R. Sreenivasan, and V. Yakhot, *New J. Phys.* **9**, 89 (2007).
- [84] J. Jimenez, *J. Fluid Mech.* **409**, 99 (2000).